coatings

MDPI

Article

Effect of Molybdate on Corrosion Performance of Oxide Coating Produced on 7075 Al Alloy Using PEO

Rouhollah Ghorbani [1], Maryam Rahmati [1], Keyvan Raeissi [1,*], Amin Hakimizad [2] and Monica Santamaria [3]

[1] Department of Materials Engineering, Isfahan University of Technology, Isfahan 84156-83111, Iran; r.ghorbani@ma.iut.ac.ir (R.G.); maryam.rahmati@ma.iut.ac.ir (M.R.)
[2] Yekta Mobaddel Pars Co., Science and Technology Campus, Yazd University, Yazd 89158-18411, Iran; aminhakimizad@gmail.com
[3] Electrochemical Materials Science Laboratory, Dipartimento di Ingegneria, Università di Palermo, Viale delle Scienze, Ed. 6, 90128 Palermo, Italy; monica.santamaria@unipa.it
* Correspondence: k_raeissi@iut.ac.ir

Abstract: In this research, plasma electrolytic oxidation (PEO) coatings were prepared on 7075 Al alloy in a silicate-based solution with Na_2MoO_4 additive using a unipolar waveform at constant current density. The coatings displayed micro-pores, micro-cracks, pancake-like and crater-like features, and also solidified molten oxide particles on the surface. The coatings were majorly composed of Al_2O_3 (γ, δ, and α), SiO_2 (amorphous), and MoO_3 phases, which confirms the incorporation of molybdenum in the case of additive-containing coatings. Molybdenum species were transported through cracks, channels, and micropores, as the ready access pathways into the coating and partly sealed the coating pores. The EIS technique was used to evaluate the long-term corrosion performance of the coatings up to 168 h of immersion in 3.5 wt.% NaCl solution. The results showed that the barrier action of the PEO coatings was highly enhanced by adding Na_2MoO_4 due to the higher resistance that alumina achieved to chlorine absorption and also its higher stability by the incorporation of MoO_3. The coating formed in the presence of 5 g L^{-1} Na_2MoO_4 showed the highest thickness and the lowest porosity percent (15.15%), which provided the highest corrosion performance at long immersion times.

Keywords: plasma electrolytic oxidation; 7075 Al alloy; sodium molybdate; corrosion resistance

check for updates

Citation: Ghorbani, R.; Rahmati, M.; Raeissi, K.; Hakimizad, A.; Santamaria, M. Effect of Molybdate on Corrosion Performance of Oxide Coating Produced on 7075 Al Alloy Using PEO. *Coatings* **2022**, *12*, 184. https://doi.org/10.3390/coatings12020184

Academic Editor: Tadeusz Hryniewicz

Received: 24 December 2021
Accepted: 28 January 2022
Published: 31 January 2022

1. Introduction

7075 aluminum alloy is widely used for aerospace and automotive industries due to a combination of properties, such as high strength-to-weight ratio, high fracture toughness, and good shape-ability. However, the weak corrosion resistance, particularly intergranular and pitting corrosion, represents a significant obstacle for its applications and has largely confined the broad use of 7075 aluminum alloy in some industries [1,2].

A naturally occurring passive oxide layer can be imparted corrosion resistance exposed to the atmosphere, but it cannot protect the Al alloy in harsh environments, such as marine or acidic environments [3]. Plasma electrolytic oxidation (PEO) has been considered as one of the most suitable surface treatments for generating a conformal oxide layer on the surface of various valve metals to improve their mechanical and electrochemical properties for industrial applications. PEO process is an anodic oxidation treatment applied above the breakdown voltage, with the consequent onset of short-lived discharges on the coating surface melting the substrate and the oxides simultaneously, which provide thick, uniform, and very adhesive coatings. The most attractive advantage of the PEO process is it is environmentally friendly, providing hard oxide ceramic layers with excellent corrosion and wear resistance and good electrical and thermal properties.

PEO coating properties are affected by processing parameters, such as the electrolyte composition, voltage, current density, waveform, and process time. Among them, the composition of the electrolytic baths plays a key role and affects the structure, phase

composition, and element distribution in a PEO coating [4]. The use of rare earth salts and metal oxides, especially cerium, lanthanum, and molybdenum, has positive effects on corrosion resistance [5]. Arunnellaiappan et al. [6] reported that the corrosion performance of 7075 Al alloy would be improved remarkably by CeO_2 particles incorporation.

Molybdate is well known as a green corrosion inhibitor when present in the electrolyte as MoO_4^{2-} and Mo (VI) ions [7–9]. Because of its strong oxidation character, its reduction product is stable and can form a passive film on metals and shift the corrosion potential to nobler values. Molybdate also acts as an oxidant, such as chromate, in the chemical conversion processes, and its adsorbed products can inhibit the penetration of Cl^- ions to protect the substrate [10,11]. The inhibitive effect of molybdate on the corrosion of Al alloys has been the subject of several papers [11–13]. Wiggle et al. [7] studied the effect of molybdate on the pitting corrosion of two Al alloys, AA3003 and AA7072, and found that the corrosion potential becomes nobler, increasing monotonically with the concentration of molybdate ions.

Recently, molybdate salt as an additive has been used for magnesium and aluminum alloys to improve corrosion resistance during PEO treatment. Wang et al. [14] studied the structure and corrosion resistance of the coatings formed on ZL108 Al alloy in the silicate-Na_2MoO_4 electrolyte using the PEO process at different current densities. The results showed that the coatings were mainly composed of mullite, γ–Al_2O_3, SiO_2, MoO_2, and MoO_3. The microstructure of the coatings and corrosion performance was significantly affected by increasing current density. Kaseem et al. [15] also investigated the effect of current frequency on the structural features and electrochemical response of MoO_2–Al_2O_3 hybrid oxide films formed on Al-Mg-Si alloy. Numerous studies have investigated the synergistic effect of molybdate with tungstate [16], ZrO_2 [17], and TiO_2 [18] on tribological [3] and corrosion properties. Usually, the effect of molybdate on PEO coatings was found at a constant molybdate concentration and the effect of molybdate concentration in the bath solution and also the distribution of Mo in the coating layers were not found. Moreover, the effect of molybdate on the long-term corrosion behavior of the PEO coatings was not reported.

This paper studies the PEO process of 7075 Al alloy in a silicate-based electrolyte containing Na_2MoO_4 to evaluate the change in microstructure, composition, and long-term corrosion performance of the prepared coatings. The incorporation mechanism is considered to explain how the different species inside the electrolytic bath are incorporated in the coating and what their role is in coating microstructure and corrosion barrier properties.

2. Materials and Methods

2.1. Specimen Preparation

Disc-shape specimens of 7075 aluminum alloy with chemical composition (wt.%) of 2.45 Mg, 5.55 Zn, 0.16 Mn, 1.20 Cu, 0.37 Si, 0.33 Fe, 0.25 Cr, and balance Al, with a diameter of 20 mm and thickness of 5 mm, were prepared from T6 heat-treated bars and used as the substrate for PEO treatment. Both flat faces of the specimens were mechanical polished using silicon carbide (SiC) from 320 to 1200 grit. Then, they washed in deionized water and ultrasonically degreased in pure ethanol, and finally dried in cold airflow. Each specimen is connected to a copper wire used as the anode in the PEO treatment.

2.2. Plasma Electrolytic Oxidation Coating Procedure

PEO treatment was performed in a cylindrical cell (with 7 L volume) made from 316 L stainless steel, while the internal cell walls were used as the cathode. The electrolytic bath contained 3 g L^{-1} sodium metasilicates ($Na_2SiO_3 \cdot 5H_2O$), 2 g L^{-1} potassium hydroxide (KOH), and 0, 3, and 5 g L^{-1} sodium molybdate (Na_2MoO_4) as an additive. The electrolyte was stirred with a submersible centrifugal pump and cooled using a water bath equipped with a chiller to keep the cell temperature at 24 ± 1 °C. Furthermore, the pH and conductivity of the bath solutions were measured using a pH-meter (AZ instrument model:

827 digital pH lab) and a digital conductometer (SCHOTT GERATE CG 857, Labexchange, Burladingen, Germany), respectively.

The specimens were coated using a full-switching power supply equipped with a double isolated source (IGBT-based pulser). The coating process was performed in 60 min using a unipolar waveform at a frequency of 2 kHz, 20% duty cycle, with the average anodic current density of 6 A dm^{-2}. During the PEO treatment, the potential-time responses were recorded. The pH and conductivity of the electrolytic baths, the codes of the coated specimens, and the coating visual appearance are shown in Table 1.

Table 1. Sample codes, pH, conductivity, and coating visual appearance of the coatings produced in various baths with different amounts of Na_2MoO_4.

Sample Code	Na_2MoO_4 (g L^{-1})	pH	Conductivity (mS·cm^{-1})	Visual Appearance
Mo-0	0	12.5	7.08	
Mo-3	3	12.42	8.96	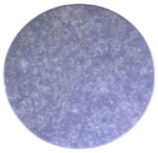
Mo-5	5	12.4	9.4	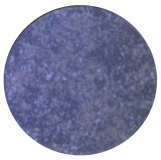

2.3. Coatings Characterization

A field emission scanning electron microscope (FESEM, FEI model Quanta FEG 450, FEI, Hillsboro, OR, USA) was applied to observe the surface and cross-section of the coatings. The chemical composition and elemental maps of the coatings were evaluated by an energy dispersive spectrometer (EDS, Octane Elite, Ametek, Mahwah, NJ, USA). The cross-section of the coatings was prepared through a grinding procedure using abrasive SiC papers up to 2400 grit. Then, the samples were polished using 0.5 microns Al_2O_3 particles. Finally, the samples were washed in deionized water, cleaned ultrasonically in ethanol, and dried in cold airflow. The average surface roughness (Ra) was measured using a stylus profilometer instrument (model Mitutoyo SJ210, Mitutoyo, Kawasaki, Japan). The thickness and porosity of the coatings were evaluated from the FESEM cross-sectional images by Image J 1.44p and MIP student software, respectively. The coating phase composition was detected using a glancing incident beam X-ray diffraction instrument (GIXRD, model ASENWARE AW-XDM300, Asenware, Shenzhen, China) by Cu Kα radiation generated at 40 kV and 30 mA. The X-ray diffraction patterns were obtained over the 2θ range of 10–80° with a step size of 0.05° and time per step of 5 s. The beam incident angle was 10°. X'pert Highscore software (Version 3.0.0) with powder diffraction file for inorganic materials (PDF2) database was used for data analysis.

2.4. Evaluation of Corrosion Performance of the Coatings

The electrochemical impedance spectroscopy (EIS) tests at long-term immersions in 3.5 wt.% NaCl, adjusted at pH 4 by adding dilute HCl solution, were performed to evaluate the barrier performance of the coatings by a potentiostat/galvanostat (model PARSTAT

2273, AMETEK, Oak Ridge, TN, USA). On the one face of the coated samples with 1.77 cm^2 area, a platinum plate and an Ag/AgCl electrode were applied as the working, counter, and reference, respectively, in a three-electrode cell. The frequency range from 100 kHz to 100 mHz and ±10 mV peak-to-peak voltage amplitude versus OCP were used for the measurements. For evaluating the performance of the coatings in aggressive solution, the EIS measurements were continued for 168 h using duplicate samples. The Power Suite and Zview software were applied to extract and fit the EIS data, respectively.

3. Results and Discussion

3.1. Voltage–Time Responses

Figure 1 shows the voltage vs. time response read during the PEO process in the baths containing 0, 3, and 5 g L^{-1} Na_2MoO_4 at 6 A dm^{-2}. In the voltage–time transients (Figure 1), four different stages can be detected.

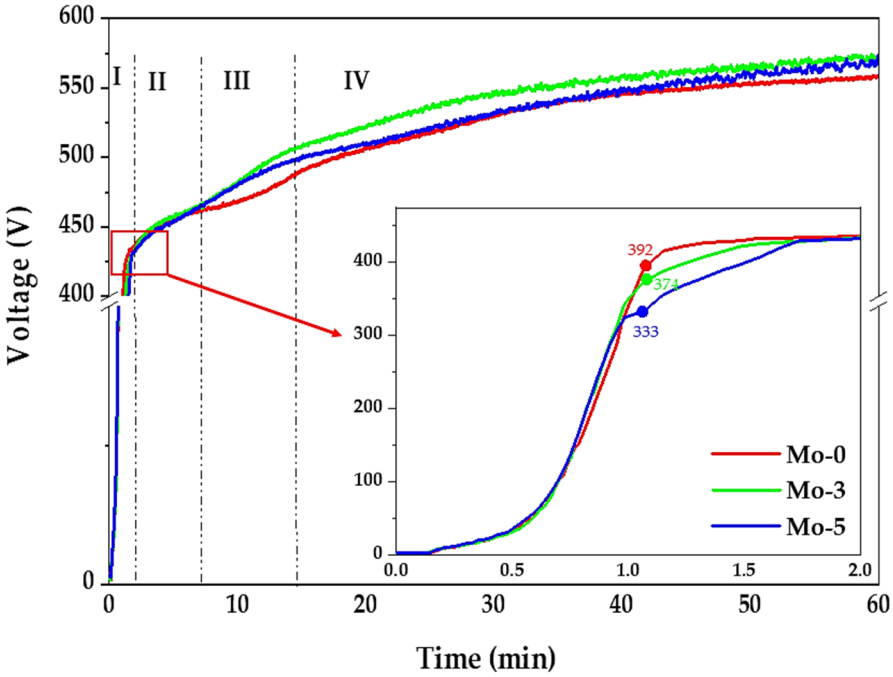

Figure 1. Voltage vs. time responses during PEO treatments in baths containing various amounts of Na_2MoO_4.

In the first stage (0–60 s), by applying the current density of 6 A dm^{-2}, the voltage increases with a very steep slope (stage I), which mainly involves the rapid electrochemical formation of a first insulating oxide film. In stage II (60–420 s), dielectric breakdown starts to occur, accompanied by numerous fine white sparks moving rapidly and uniformly over the entire sample surface. The addition of Na_2MoO_4 in the solution increased the conductivity. The values of the breakdown voltage depend upon the solution conductivity and decrease with increasing the value of conductivity [19,20]. Thus, the lowest breakdown voltage is achieved in the solution with 5 g L^{-1} Na_2MoO_4 showing the highest conductivity of 9.40 mS cm^{-1}. In this stage, voltage increases nonlinearly with time, with a gentle slope, by forming a more compact and thicker oxide layer. In stage III, intensive discharges, such as orange glow, are observed, which are randomly distributed on the sample surface via slow-moving [21]. In this stage, the second inflection is defined as the critical voltage occurs. Then, the cell voltage (stage IV) reaches a relatively stable value, and gradually the spark size and intensity increase. This voltage–time transient is recorded for both PEO processes with and without molybdate.

3.2. Surface Morphology Observation and Roughness of the Coatings

The FESEM micrographs in Figure 2 show the surface morphology and roughness of the coatings. The micro-pores, micro-cracks, pancake-like, crater features, and solidified molten oxide particles were observed on the surface of all coatings. The oxide granules and micro-pores are mainly originated from ejected materials, random discharging, and gas entrapping [22]. In addition, the pancake and crater features are formed due to the ejection of molten aluminum from the substrate/coating interface along with the molten alumina from the inner/outer layer interface through the B-type and E-type discharge channels, respectively. As soon as the molten Al reaches the coating/electrolyte interface, it is oxidized and solidified, forming the pancakes [23,24]. The rapid solidification of molten oxide when it is surrounded by the solution develops the thermal stresses leading to micro-cracks. The difference between thermal coefficients of oxide layer and substrate and also the high pressure governed during the PEO process enhance the number of micro-cracks [25,26].

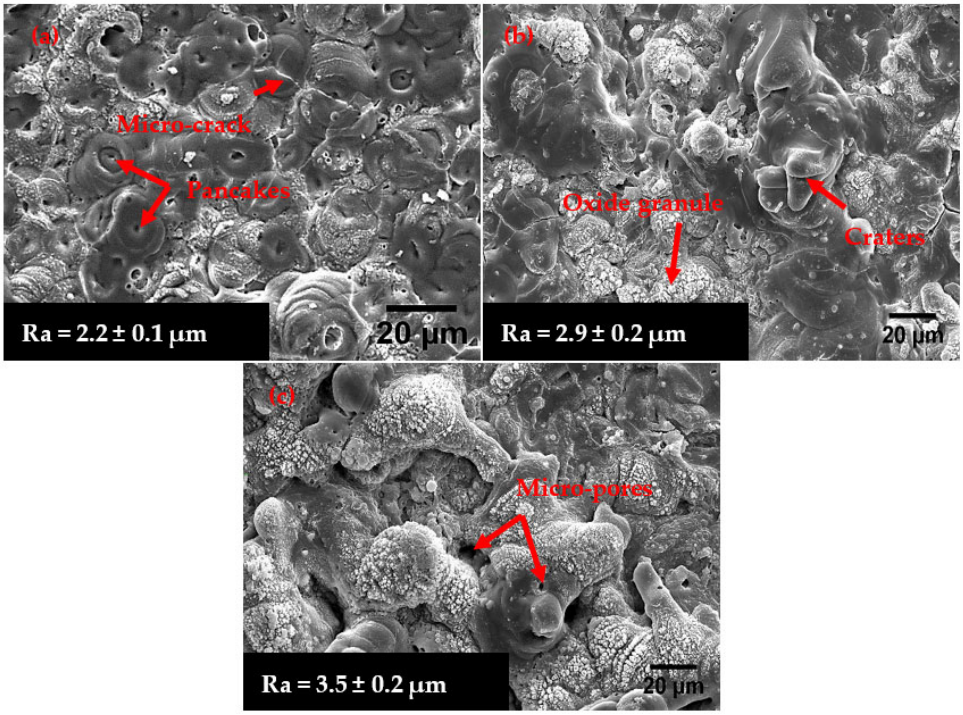

Figure 2. FESEM surface morphology images of the coatings prepared in solutions containing different Na_2MoO_4 concentrations: (**a**) Mo-0, (**b**) Mo-3, and (**c**) Mo-5.

As the Na_2MoO_4 concentration in electrolyte increases, the density of oxide granules is increased, and the pancake features are decreased due to the reduction of strong discharges and the increment of A and C-type discharges, confirmed by decreasing breakdown voltage. Therefore, the surface morphology of the coatings seems rougher with increasing Na_2MoO_4 concentration (as seen in Figure 2c). Moreover, it seems that the diameter and number of the micropores on the coating surface decreased with increasing Na_2MoO_4 concentration [3].

As seen in Figure 2, the Ra increases with incrementing concentration from 0 to 5 g L^{-1}, which is also in agreement with the FESEM images. The higher final voltage results in a coarse microstructure [27,28]. Furthermore, the high tendency formation of crater features and granules of oxide compounds increases the surface roughness. The Mo-5 has the highest Ra with the highest final voltage.

3.3. Cross-Sectional Observation, Structure, and Composition of the Coatings

Figure 3 displays cross-sectional images of the coatings. Typically, PEO coating comprises up to three sub-layers, including a dense inner layer, a region with accumulated

pores in the form of a pore band, and a more compact outer layer penetrated by discharge channels [29]. The inner layer adjacent to the substrate is very thin and displays a wavy-jagged appearance, which makes them an integral part of the substrate as the result of substrate dissolution at the early stage of the PEO process when discontinuous oxidation of the aluminum substrate occurs [30,31]. The middle layer involving porosity is orientated parallel to the substrate surface and originated due to the occurrence of D-type discharge. Moreover, the cross-sections show that the coated samples are composed of both micro-cracks and micro-pores, originating from various discharge types and thermal stresses.

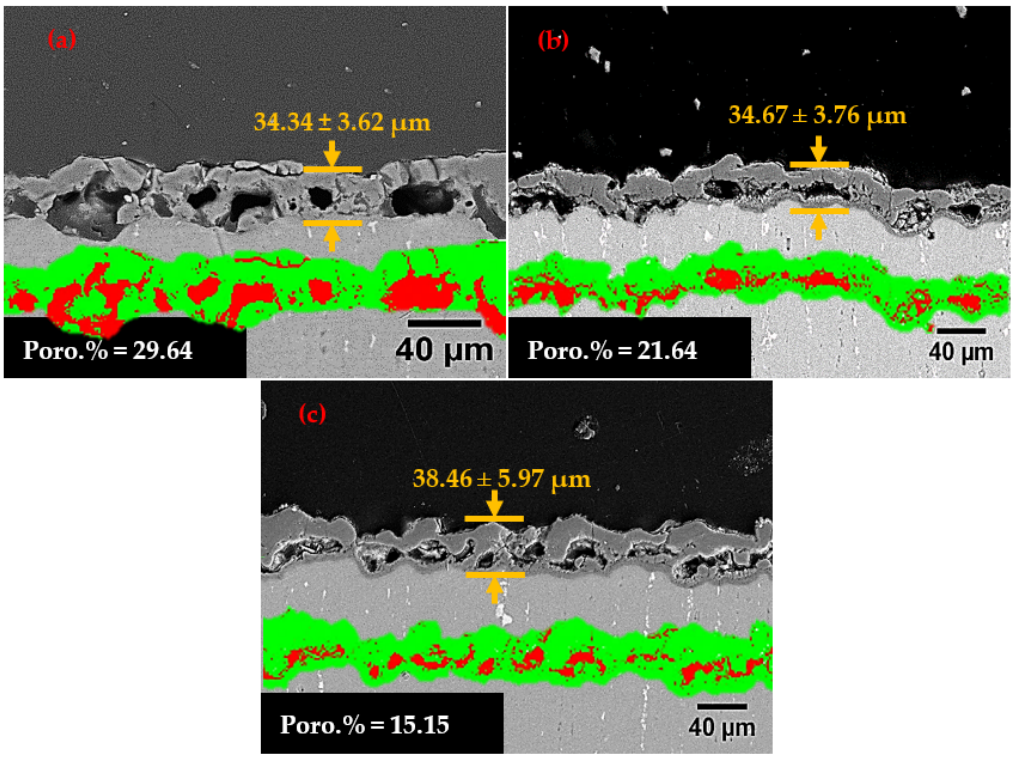

Figure 3. FESEM cross-sections of the coatings prepared in the presence of various Na_2MoO_4 concentrations: (**a**) Mo-0, (**b**) Mo-3, and (**c**) Mo-5. The images inserted below of each cross-sectional view demonstrate the porosity percentage (red areas) using MIP software.

The average thickness values of the PEO coatings were estimated from cross-sectional images using Image J software and are shown in Figure 3. According to Figure 3, the average thickness of the coating grown in the bath with no Na_2MoO_4 content (Mo-0) is 34.3 ± 3.6 µm, while with the addition of Na_2MoO_4, the average thickness increases. It is 38.5 ± 5.9 µm for the coating produced in 5 g L^{-1} Na_2MoO_4 solution (Mo-5). As the concentration of sodium molybdate increases, the formation of Mo^{6+} ions increases, which increases the coating thickness and encourages a more passivation process [7]. The non-uniform distribution of discharges and higher aggressiveness of solution with the increasing of the Na_2MoO_4 concentration supports the higher coating thickness by the continually local thickening of the coating followed by breakdown events and substrate dissolution [7,32]. The increase of the coating thickness raises the surface roughness, as confirmed by the profilometry results (Figure 2). This is due to the increase in required energy for the current to pass from the thicker coating. Consequently, the diameter of the discharge channels and molten oxide eruption increases, resulting in a higher surface roughness [33].

The porosity percent of the PEO coatings, measured from FESEM cross-sectional images using MIP software, is inserted in Figure 3. The porosity percent decreases with increasing the Na_2MoO_4 concentration due to the higher Pilling–Bedworth ratio (RPB) of MoO_2 and MoO_3 (2.94 and 3.38, respectively) than Al_2O_3 (1.28) [14,34]. On the other

hand, the lower breakdown voltage of the Mo-5 specimen reduces the destructive micro-discharges and decreases the porosity percent. Therefore, the presence and increasing the concentration of Na_2MoO_4 salt in electrolytic bath decreases the porosity of PEO coatings.

Figure 4 shows the distribution maps of elements in the coating cross-sections. As seen, the Al from the substrate is distributed uniformly throughout the coatings. The Si from the electrolyte is found mainly on the top surface of the outer layer due to the occurrence of A and C-type discharges [23]. Moreover, Si exists mostly inside the pore walls located in the middle layer. In the coatings containing Na_2MoO_4, Mo shows an even distribution across the coating thickness, while the accumulation of Mo is observed in the inner layer and the micro-pores.

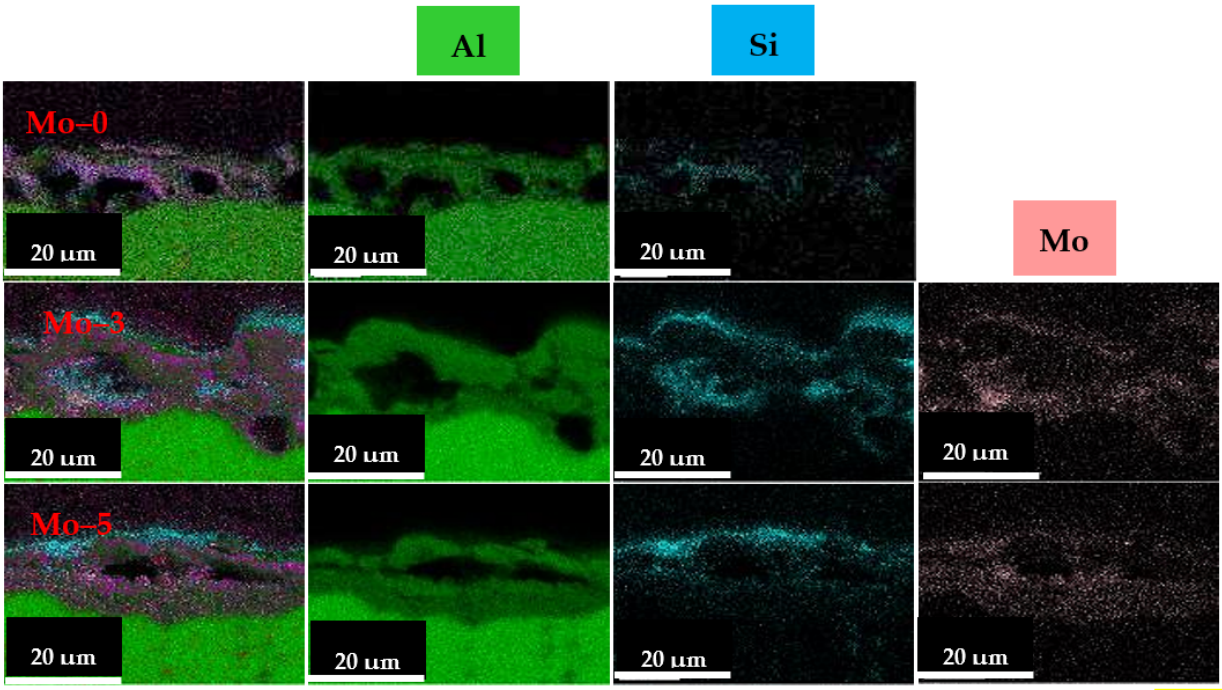

Figure 4. The elemental maps on the cross-section of the PEO specimens prepared in the silicate-based solution with and without additive at various Na_2MoO_4 concentrations that consist of Al, Si, and Mo elements marked by green, blue, and pink colors, respectively.

Atomic percentages (at.%) of the elements taken from selected areas on the cross-section of the coatings and also at micro-pore walls (shown in Figure 5) using EDS analysis are listed in Table 2. The Si content of the coating is decreased by adding Na_2MoO_4 to the bath and increases with an increasing Na_2MoO_4 concentration. As the Na_2MoO_4 concentration increases, the value of Mo also increases in the coatings. It is worth noting that Mo tends to be accumulated in the vicinity and inside of the micro-pores of the coatings (as seen in EDS analysis for selected area 2 in Figure 5b,c), due to high surface energy, which reduces the ionic mobility of Mo ions [15].

According to previous papers [17], Na_2MoO_4 salt added in the bath dissociates based on the following reaction:

$$Na_2MoO_4 \rightarrow 2Na^+ + MoO_4^{2-} \quad (1)$$

The incorporation of MoO_4^{2-} ions mainly occurs by migration during the anodic cycles under the electrical field and form the MoO_2 and MoO_3 phases by the chemical anodic reaction. Monfort et al. [35] suggested that the species of electrolytes are distributed and incorporated with different separate routes. Molybdenum species, such as phosphorus species, may be transported along short-circuit paths, such as grain boundaries, cracks, channels, and micropores, which provide ready access to the inner part of the coating

and make the pores semi-sealed [35]. Figure 6 shows a schematic image explaining the incorporation mechanism of MoO_4^{2-} and SiO_3^{2-} anions during the PEO process. As seen, up-taking the MoO_4^{2-} and SiO_3^{2-} anions into coating mainly occurs through adhering on the melting pools obtained by the discharging events during the PEO process and electrostatic adsorption due to the applied negative charge. During discharging events, MoO_4^{2-} ions can enter the channel by the electric field, and the local melting promoted by the heat of sparking is responsible for sintering [36]. The lower melting point of MoO_2 and MoO_3 (1100 and 795 °C, respectively) compared to the melting point of Al_2O_3 (about 2000 °C) and other possible phases, such as $Al_6O_{13}Si_2$ and SiO_2 (1880 and 1710 °C, respectively), facilitates the sintering process. MoO_2 and MoO_3 phases are inertly incorporated into the coating due to their high thermodynamical stability [37].

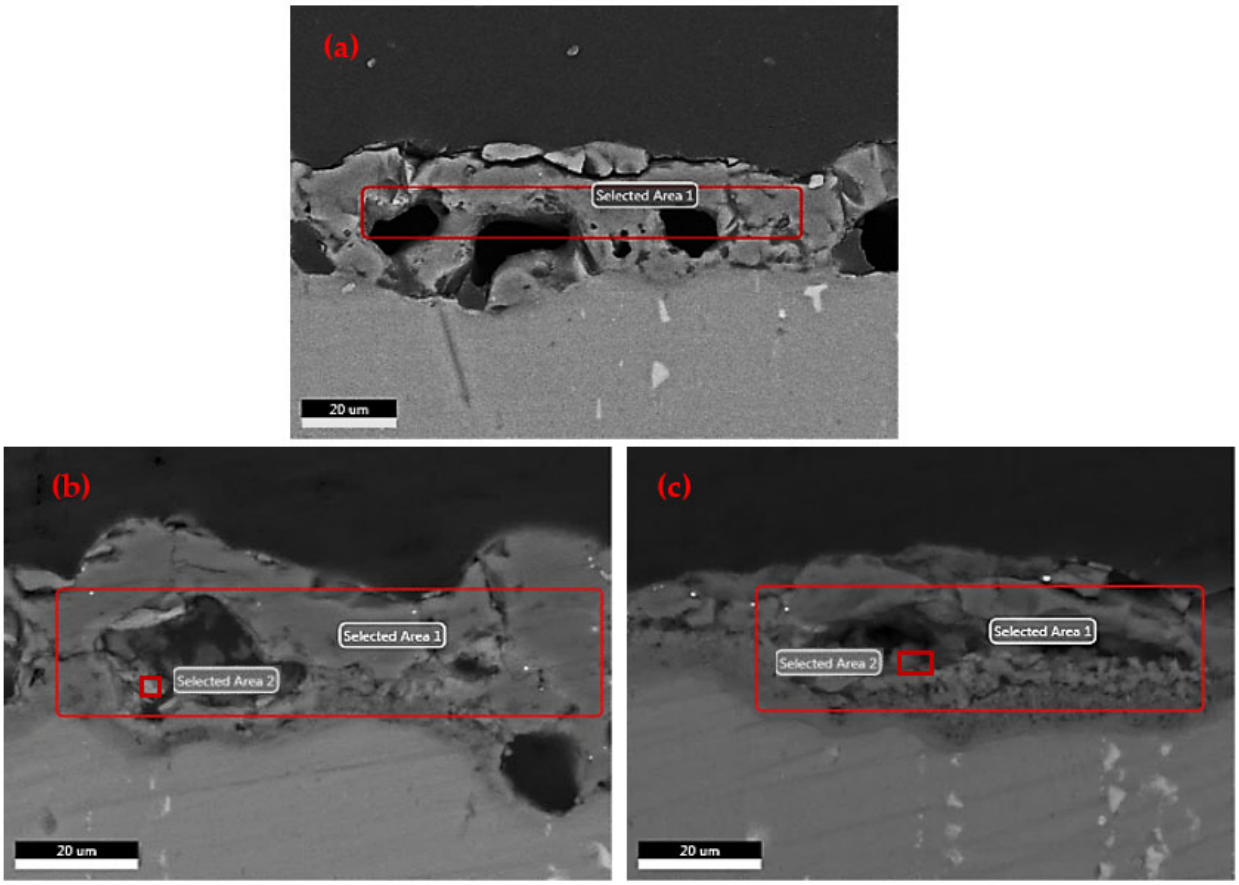

Figure 5. The selected areas from a cross-section of the coatings and micro-pore for EDS analysis: (**a**) Mo-0, (**b**) Mo-3, and (**c**) Mo-5.

Table 2. EDS analysis results of the coatings.

Sample	Element (at.%)							
	Selected Area	Al	Mg	O	Mo	Si	Na	K
Mo-0	1	41.83	0.72	45.92	-	8.77	1.74	1.03
Mo-3	1	41.22	0.51	53.27	0.43	4.25	0.27	0.04
	2	23.42	0.12	64.71	3.93	7.05	0.60	0.18
Mo-5	1	43.44	0.61	52.91	0.56	2.09	0.30	0.09
	2	35.72	0.40	55.92	4.54	3.03	0.34	0.04

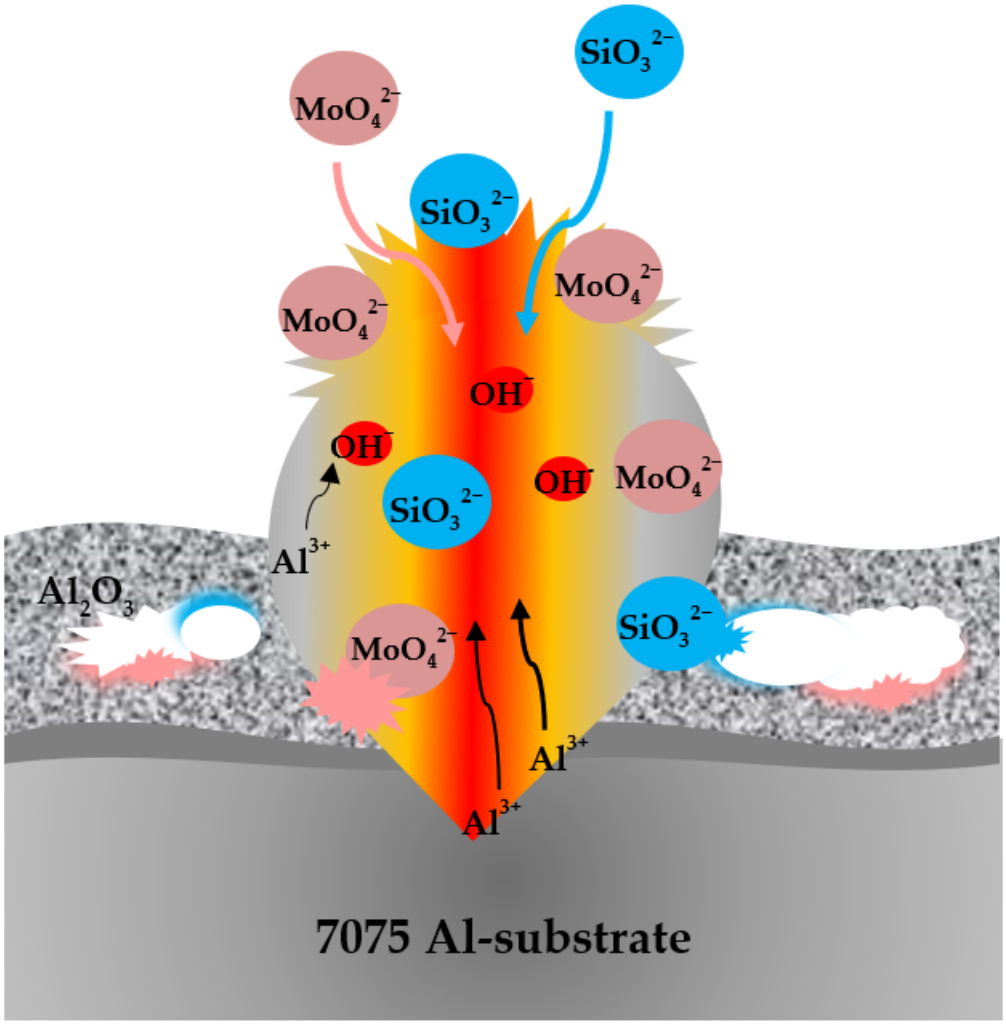

Figure 6. Schematic image from the incorporation of MoO_4^{2-} and SiO_3^{2-} anions in plasma discharging and the resulted structure of the coating.

3.4. The Phase Composition of the Coatings

Figure 7 shows XRD patterns of the coatings obtained in the solutions containing various Na_2MoO_4 concentrations. The coatings formed are mainly composed of alumina with different allotropy of γ-gamma, δ-delta, and α-alpha (γ–Al_2O_3–ICDD PDF no. 10–0425, δ–Al_2O_3–ICDD PDF no. 04–0877, and α–Al_2O_3–ICDD PDF no. 46–1212). The nuclei of γ–Al_2O_3 could directly originate from molten oxide under 1473 °C and supercooling during the PEO process [38]. The transformation of the γ–Al_2O_3 to the α–Al_2O_3 phase needs tremendous energy provided by micro-discharging to overcome the energy barrier [39]. The transforming drive force increases with the temperature rise. The presence of diffraction peaks of α–Al_2O_3 in the coatings indicates that the magnitude of the applied current density and reaction times are sufficient to support the phase transformation. The coatings formed in the bath containing Na_2MoO_4 show the obvious peaks with low diffraction intensity corresponding to molybdenum oxide (MoO_3–ICDD PDF no. 21–0569) in addition to the above-mentioned phases, which reconfirms the incorporation of molybdenum into the coatings. The diffractions relating to Al (ICDD PDF no. 85–1327) from the substrate are also evident but decrease with the increase of thickness and decrease of porosity of the coating by the increasing Na_2MoO_4 concentration. The patterns also show a halo in the 2θ range of 20–45°, denoting an amorphous phase, which should be mostly SiO_2. It was reported that the silicon may be incorporated in the coating by transport, respectively, in lattice or network sites of the crystalline and amorphous regions of the coating [35,40].

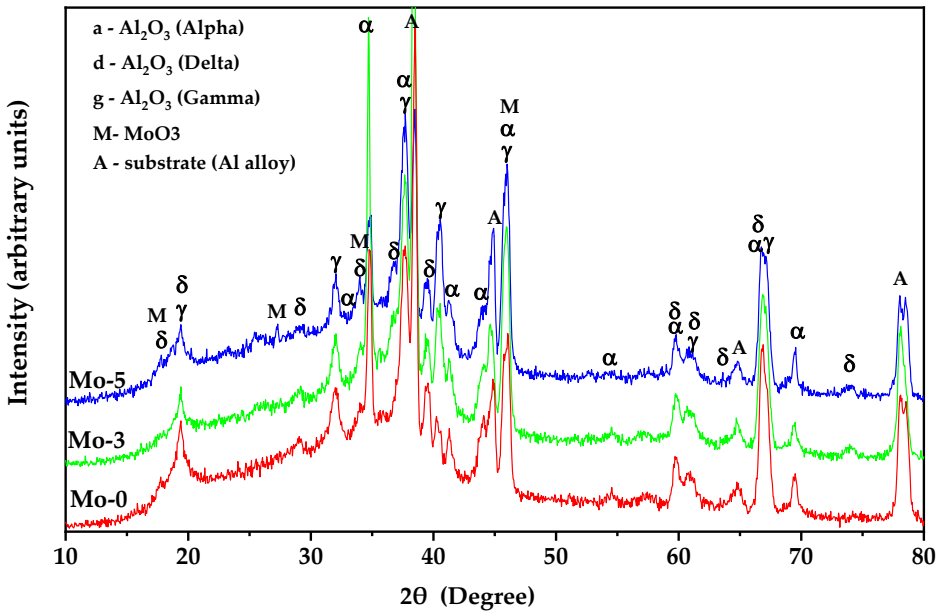

Figure 7. XRD patterns of the PEO coatings grown at various Na_2MoO_4 concentrations.

3.5. Long-Term Electrochemical Impedance Spectroscopy (EIS) Measurements

To evaluate and compare the long-term corrosion performance of the coatings, the EIS tests were performed in 3.5 wt.% NaCl solution (pH 4 ± 0.1) after 24, 48, and 168 h of immersion. The Nyquist and Bode-phase diagrams of the samples after different immersion times are shown in Figure 8. After 24 h of immersion, a two-time constant response with two humps can be seen in Bode-phase plots (Figure 8a′), which confirms the dual structure of the coatings [29]. The humps at low frequencies are related to the dense inner layers of the coatings, and those at high frequencies result from the porous outer layers. Correspondingly, in the Nyquist diagrams (Figure 8a), large and small capacitive loops indicate that the coatings have barrier functions against the aggressive solution to penetrate toward the middle layer (pore band-like) and substrate, respectively. With an increase in the immersion time to 48 h, the values of phase angle at the high frequencies decrease (Figure 8b′), which is related to the decrease of barrier resistance of the outer layer due to the penetration of aggressive solution inside the pores of the coatings [41,42]. After 168 h of immersion, the humps are merged to be flattened, as seen in Figure 8c′. In the Nyquist diagrams (Figure 8c), the Mo-5 sample shows the largest capacitive loop.

The best appropriate equivalent circuit (EC) model for fitting the EIS data is shown in Figure 9. In this EC model, R_s correspond to the resistance of solution, R_{out} and CPE_{out} represent the resistance and constant phase element of the outer layer, and R_{in} and CPE_{in} explain the resistance and constant phase element of the inner layer of the coatings. The constant phase element is introduced due to the non-ideal capacity behavior of the outer and inner layers. The black lines in Figure 8 represent the fitting curves, and the best-fitting parameters ($\chi^2 < 0.003$) are summarized in Table 3.

According to the fitting data (Table 3), after 24 h, the maximum R_{out} value is for Mo-3 coating, which is probably caused by the sufficient sealing provided by MoO_3 particles in the outer layers of the coatings. With an increase in the immersion time, the R_{out} values are decreased, and their values become negligible for all coatings. The obtained results from the fitting data show that the R_{in} values are significantly higher than the R_{out} ones. Thus, the corrosion performance of the PEO coatings is mostly determined by their inner layer resistances. The dependence of R_{in} versus immersion time is drawn for the coatings in Figure 10. As seen, the Mo-0 coating shows the highest R_{in} value at the beginning of immersion. After 48 h, R_{in} values of the coatings fall, especially for the Mo-0 specimen. For this specimen, it is assumed that the R_{in} is strongly reduced due to its lower thickness

and higher porosity. The decay in R_{in} is due to the up-taking of the corrosive solution through the pores of the middle layer, which touches the inner layer of the coating. For Mo-containing coatings, R_{in} is less affected by immersion time, and, notably, it even increases for Mo-5 at long immersion times. It is reported that aluminum oxides containing molybdenum are not stable at low pH (pH 4), and their preferential dissolution substantially changes the composition, making them richer in Mo(IV) compound (MoO_3 and $MoO(OH)_2$) at enough exposure time, which are more stable in acidic solutions [8]. Therefore, the increase of Mo content on the coating surface is responsible for better barrier properties. On the other hand, the aluminum oxide film, which contains molybdenum oxide, resists chlorine absorption because molybdenum oxide reduces the pH of aluminum oxide at the point of zero charges (isoelectric point) (from 9–9.5 to 3–6) [43]. This oxide film provides corrosion inhibition within the pH range 3–6 [7]. It was reported that MoO_4^{2-} ions are classified as anodic inhibitors and affect both general and pitting corrosion [44]. As a result, the Mo-5 coating has the highest barrier performance in long-term immersion, not only due to its higher thickness and lower porosity but also due to the higher molybdenum content.

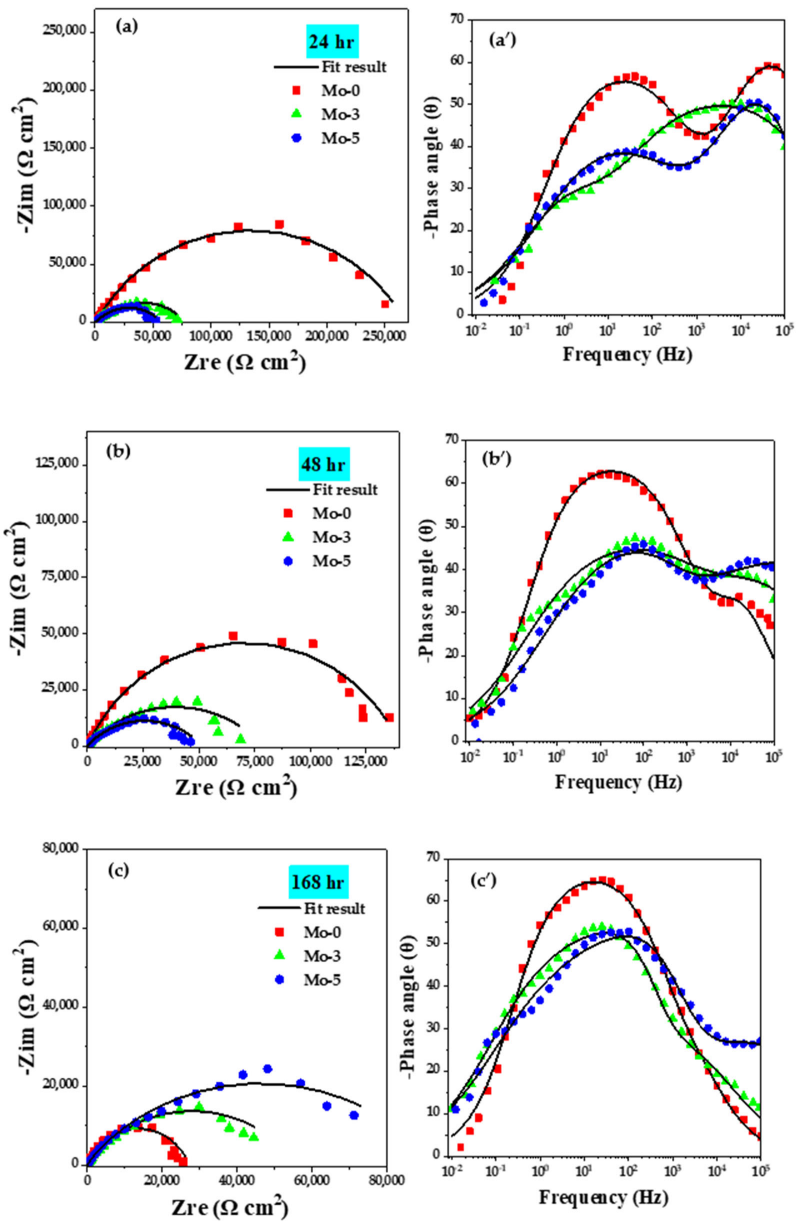

Figure 8. Nyquist and Bode-phase plots of the coated samples after long-term exposure to 3.5 wt.% NaCl solution for: (**a**,**a**′) Mo-0, (**b**,**b**′) Mo-3, and (**c**,**c**′) Mo-5.

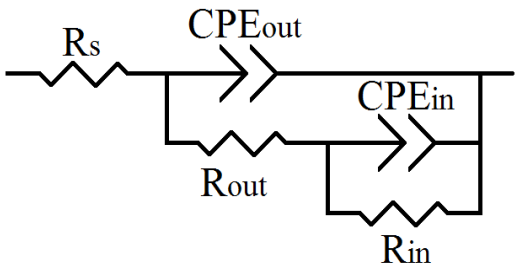

Figure 9. The electrical equivalent circuit was used for fitting the EIS data.

Table 3. Electrical elements extracted from EIS plots using Zview software for Mo-0, Mo-3, and Mo-5 specimens.

Specimens	Immersion Time	Outer Layer			Inner Layer		
		CPE_{out} ($\mu F\ cm^{-2}\ S^{n-1}$)	n_{out}	R_{out} ($k\Omega\ cm^2$)	CPE_{in} ($\mu F\ cm^{-2}\ S^{n-1}$)	n_{in}	R_{in} ($k\Omega\ cm^2$)
Mo-0	24 h	0.22	0.79	1.82	1.87	0.67	266.05
	48 h	1.33	0.76	0.27	4.23	0.74	139.97
	168 h	16.35	0.76	0.07	11.23	0.77	27.18
Mo-3	24 h	3.53	0.59	19.79	11.16	0.56	57.69
	48 h	9.47	0.51	1.66	2.17	0.6	77.5
	168 h	27.55	0.56	0.49	1.27	0.91	56.13
Mo-5	24 h	0.51	0.74	1.41	11.75	0.52	56.42
	48 h	9.98	0.5	2.21	1.63	0.67	49.62
	168 h	14.25	0.5	0.38	1.56	0.79	94.55

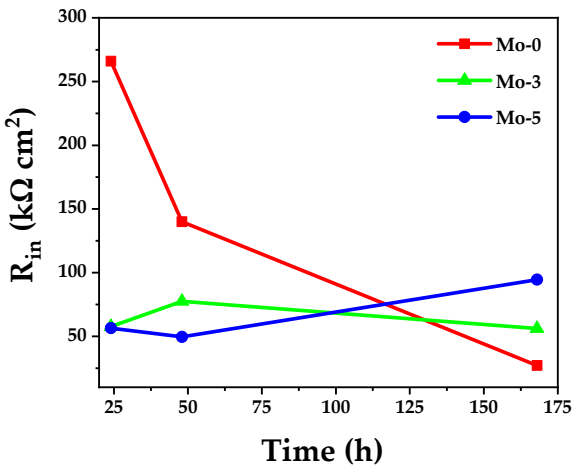

Figure 10. The variation of R_{in} versus immersion time for the PEO coatings.

Figure 11 shows the surface morphologies and the elemental distribution maps of the coatings after 168 h of immersion in the corrosive solution. All the coating surfaces show holes of different sizes due to localized attacks initiating at the weakest points of the coatings. Fewer damages appear for the sample coated in the solution containing 5 g L^{-1} Na_2MoO_4. However, the absence of inductive loops in Nyquist curves indicates that these holes have no connection to the substrate and have not caused corrosive electrolyte contact with the substrate surface [45,46]. The elemental distribution maps show that the Cl^- ions' adsorption decreases with increasing Na_2MoO_4 concentration. Molybdate can inhibit the penetration of Cl^- ions to protect the coatings and substrate, as described by refs. [10,11].

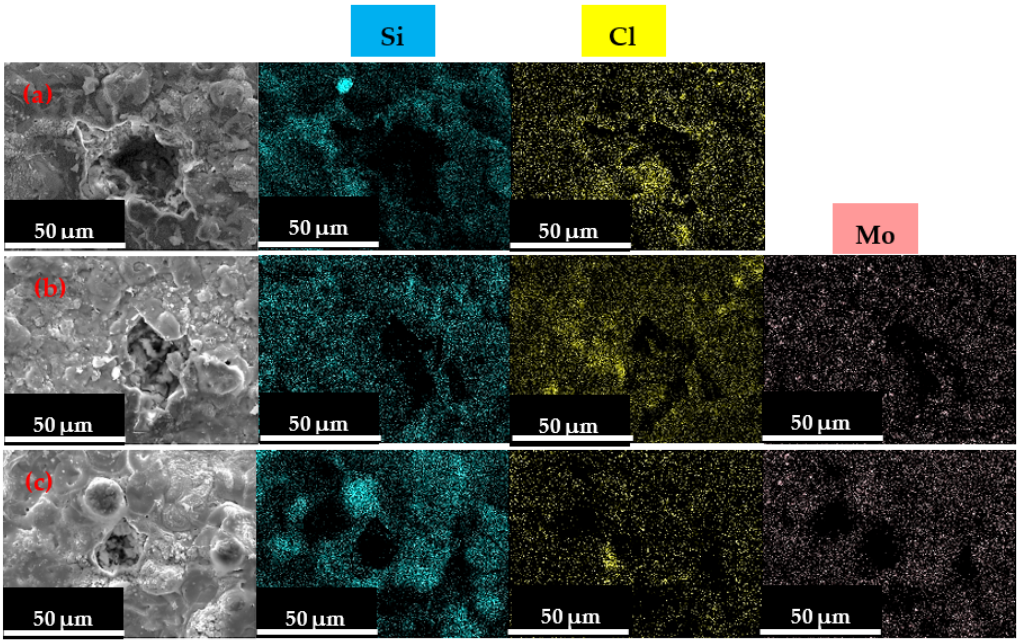

Figure 11. Surface morphology and the elemental maps of the coated specimens after 168 h of immersion in 3.5 wt.% NaCl solution for: (**a**) Mo-0, (**b**) Mo-3, and (**c**) Mo-5.

4. Conclusions

Plasma electrolytic oxidation of 7075 Al alloy in an alkaline silicate-based solution with different amounts of Na_2MoO_4 was performed using a unipolar waveform. The following results were obtained:

1. The incorporation of Mo into the coating lowered the voltage-time response thanks to increasing the electrolyte conductivity and hence decreasing the breakdown voltage and intensity of micro-discharging.
2. The coating's average thickness was increased by raising the Na_2MoO_4 content. The highest porosity percentage (i.e., 29.64%) was calculated for the coating with no Mo content, while the lowest (i.e., 15.15%) was achieved for the specimen with the highest Mo content.
3. Based on EDS analysis and elemental map, Mo tends to be accumulated in the vicinity and inside of the micro-porosity. The finer discharging channels were sealed due to the formation of molybdenum oxides. Further, Mo is transported to the inner parts of the coating, which further improves its barrier property.
4. The coating produced in 5 g L^{-1} Na_2MoO_4 solution displayed the highest barrier performance at long-term immersion due to the higher stability of aluminum oxide rich in molybdenum oxide, higher resistance to chlorine absorption, the highest thickness, and lowest porosity. The semi-sealed pores have also hindered the aggressive solution from touching the substrate surface, preventing the local attack on the substrate.

Author Contributions: Conceptualization, R.G., K.R. and M.S.; methodology, R.G., K.R. and A.H.; software, R.G. and M.R.; validation, R.G., M.R., K.R., A.H. and M.S.; formal analysis, R.G. and M.R.; investigation, R.G.; resources, R.G.; data curation, R.G.; writing—original draft preparation, R.G. and M.R.; writing—review and editing, K.R. and M.S.; visualization, R.G., M.R. and K.R.; supervision, K.R.; project administration, K.R. All authors have read and agreed to the published version of the manuscript.

Funding: This research received no external funding.

Institutional Review Board Statement: Not applicable.

Informed Consent Statement: Not applicable.

Data Availability Statement: Data sharing not applicable.

Acknowledgments: Supports by Plasma Oxide Pars Co. is acknowledged.

Conflicts of Interest: The authors declare no conflict of interest.

References

1. Toulabifard, A.; Hakimizad, A.; Di Franco, F.; Raeissi, K.; Santamaria, M. Synergistic effect of W incorporation and pulsed current mode on wear and tribocorrosion resistance of coatings grown by plasma electrolytic oxidation on 7075 Al alloy. *Mater. Res. Express* **2019**, *6*, 106502. [CrossRef]
2. Zhang, Y.; Fan, W.; Du, H.Q.; Zhao, Y.W. Corrosion Behavior and Structure of Plasma Electrolytic Oxidation Coated Aluminum Alloy. *Int. J. Electrochem. Sci.* **2017**, *12*, 6788–6789. [CrossRef]
3. Zeng, D.; Liu, Z.; Zou, L.; Wu, H. Tribological behavior of Al_2O_3-MoO_2-SiO_2 composite ceramic coating on Al-Zn-Mg-Cu alloy. *Coatings* **2021**, *11*, 915. [CrossRef]
4. Lu, X.; Mohedano, M.; Blawert, C.; Matykina, E.; Arrabal, R.; Kainer, K.U.; Zheludkevich, M.L. Plasma electrolytic oxidation coatings with particle additions—A review. *Surf. Coatings Technol.* **2016**, *307*, 1165–1182. [CrossRef]
5. Cai, J.; Cao, F.; Chang, L.; Zheng, J.; Zhang, J.; Cao, C. The preparation and corrosion behaviors of MAO coating on AZ91D with rare earth conversion precursor film. *Appl. Surf. Sci.* **2011**, *257*, 3804–3811. [CrossRef]
6. Arunnellaiappan, T.; Ashfaq, M.; Krishna, L.R.; Rameshbabu, N. Fabrication of corrosion-resistant Al_2O_3-CeO_2 composite coating on AA7075 via plasma electrolytic oxidation coupled with electrophoretic deposition. *Ceram. Int.* **2016**, *42*, 5897–5905. [CrossRef]
7. Cro, B.; Mo, B. Corrosion Behaviour of Molybdate Conversion Coated Aluminium. *J. Res. Chem.* **2011**, *4*, 1520–1525.
8. Akiyama, E.; Kawashima, A.; Asami, K.; Hashimoto, K. The corrosion behavior of sputter-deposited amorphous Al-Cr-Mo alloys in 1 M HCl. *Corros. Sci.* **1996**, *38*, 279–292. [CrossRef]
9. Vukasovich, M.S.; Farr, J.P.G. Molybdate in Corrosion Inhibition—A Review. *Mater. Perform.* **1986**, *25*, 9–18. [CrossRef]
10. Hamdy, A.S.; Beccaria, A.M.; Traverso, P. Corrosion protection of AA6061 T6-10 % Al_2O_3 composite by molybdate conversion coatings. *J. Appl. Electrochem.* **2005**, *35*, 467–472. [CrossRef]
11. Moshier, W.C.; Davis, G.D. Interaction of molybdate anions with the passive film on aluminum. *Corrosion* **1990**, *46*, 43–50. [CrossRef]
12. Kendig, M.; Cunningham, M.; Jeanjaquet, S.; Hardwick, D. Role of Corrosion Inhibiting Pigments on the Electrochemical Kinetics of a Copper-Containing Aluminum Alloy. *J. Electrochem. Soc.* **1997**, *144*, 3721–3727. [CrossRef]
13. Li, Z.J.; Yuan, Y.; Jing, X.Y. Comparison of plasma electrolytic oxidation coatings on Mg-Li alloy formed in molybdate/silicate and aluminate/silicate composite electrolytes. *Mater. Corros.* **2014**, *65*, 493–501. [CrossRef]
14. Wang, P.; Wu, T.; Guo, X.Y.; Peng, Y. Effects of Current Density on the Properties of Microarc Oxidation Coatings Formed on Aluminum Alloy in Silicate-Na_2MoO_4 Electrolyte. *Mater. Sci. Forum.* **2015**, *814*, 398–403. [CrossRef]
15. Kaseem, M.; Kamil, M.P.; Ko, Y.G. Electrochemical response of MoO_2-Al_2O_3 oxide films via plasma electrolytic oxidation. *Surf. Coat. Technol.* **2017**, *322*, 163–173. [CrossRef]
16. Thompson, G.E.; Skeldon, P.; Shimizu, K.; Wood, G.C. The compositions of barrier-type anodic films formed on aluminium in molybdate and tungstate electrolytes. *Philos. Trans. R Soc. London A* **1995**, *350*, 143–168. [CrossRef]
17. Kaseem, M.; Lee, Y.H.; Ko, Y.G. Incorporation of MoO_2 and ZrO_2 particles into the oxide film formed on 7075 Al alloy via micro-arc oxidation. *Mater. Lett.* **2016**, *182*, 260–263. [CrossRef]
18. Kaseem, M.; Ko, Y.G. Electrochemical Response of Al_2O_3-MoO_2-TiO_2 Oxide Films Formed on 6061 Al Alloy by Plasma Electrolytic Oxidation. *J. Electrochem. Soc.* **2016**, *163*, C587–C592. [CrossRef]
19. Yerokhin, A.L.; Voevodin, A.A.; Lyubimov, V.V.; Zabinski, J.; Donley, M. Plasma electrolytic fabrication of oxide ceramic surface layers for tribotechnical purposes on aluminium alloys. *Surf. Coat. Technol.* **1998**, *110*, 140–146. [CrossRef]
20. Ikonopisov, S. Theory of electrical breakdown during formation of barrier anodic films. *Electrochim. Acta* **1977**, *22*, 1077–1082. [CrossRef]
21. Duan, H.; Yan, C.; Wang, F. Growth process of plasma electrolytic oxidation films formed on magnesium alloy AZ91D in silicate solution. *Electrochim. Acta* **2007**, *52*, 5002–5009. [CrossRef]
22. Madhan Kumar, A.; Kwon, S.H.; Jung, H.C.; Shin, K.S. Corrosion protection performance of single and dual Plasma Electrolytic Oxidation (PEO) coating for aerospace applications. *Mater. Chem. Phys.* **2015**, *149*, 480–486. [CrossRef]
23. Cheng, Y.L.; Xue, Z.G.; Wang, Q.; Wu, X.Q.; Matykina, E.; Skeldon, P.; Thompson, G.E. New findings on properties of plasma electrolytic oxidation Coatings from study of an Al-Cu-Li alloy. *Electrochim. Acta* **2013**, *107*, 358–378. [CrossRef]
24. Hussein, R.O.; Nie, X.; Northwood, D.O.; Yerokhin, A.; Matthews, A. Spectroscopic study of electrolytic plasma and discharging behaviour during the plasma electrolytic oxidation (PEO) process. *J. Phys. D Appl. Phys.* **2010**, *43*, 105–203. [CrossRef]
25. Hussein, R.O.; Northwood, D.O.; Su, J.F.; Nie, X. A study of the interactive effects of hybrid current modes on the tribological properties of a PEO (plasma electrolytic oxidation) coated AM60B Mg-alloy. *Surf. Coat. Technol.* **2013**, *215*, 421–430. [CrossRef]
26. Xiang, N.; Song, R.G.; Wang, C.; Mao, Q.Z.; Ge, Y.J.; Ding, J.H. Formation of corrosion resistant plasma electrolytic oxidation coatings on aluminium alloy with addition of sodium tungstate species Formation of corrosion resistant plasma electrolytic oxidation coatings on aluminium alloy with addition of sodium tungsta. *Corros Eng Sci Technol.* **2016**, *2782*, 1743–2782. [CrossRef]

27. Shahri, Z.; Allahkaram, S.R.; Soltani, R.; Jafari, H. Optimization of plasma electrolyte oxidation process parameters for corrosion resistance of Mg alloy. *J. Magnes. Alloy.* **2018**, *8*, 1–10. [CrossRef]
28. Sikdar, S.; Menezes, P.V.; Maccione, R.; Jacob, T. Plasma Electrolytic Oxidation (PEO) Process—Processing, Properties and Applications. *Nanomaterials* **2021**, *11*, 1375. [CrossRef]
29. Ma, X.; Blawert, C.; Höche, D.; Zheludkevich, M.L.; Kainer, K.U. Investigation of electrode distance impact on PEO coating formation assisted by simulation. *Appl. Surf. Sci.* **2016**, *388*, 304–312. [CrossRef]
30. Hussein, R.O.; Northwood, D.O.; Nie, X. Processing-Microstructure Relationships in the Plasma Electrolytic Oxidation (PEO) Coating of a Magnesium Alloy. *Mater. Sci. Appl.* **2014**, *5*, 124–139. [CrossRef]
31. Liu, X.; Wang, S.; Du, N.; Li, X.; Zhao, Q. Evolution of the three-dimensional structure and growth model of plasma electrolytic oxidation coatings on 1060 aluminum alloy. *Coatings* **2018**, *8*, 105. [CrossRef]
32. Hussein, R.O.; Northwood, D.O. Improving the performance of magnesium alloys for automotive applications. *WIT Trans. Built Environ.* **2014**, *137*, 531–544.
33. Hakimizad, A.; Raeissi, K.; Golozar, M.A.; Lu, X.; Blawert, C.; Zheludkevich, M.L. Influence of cathodic duty cycle on the properties of tungsten containing Al_2O_3/TiO_2 PEO nano-composite coatings. *Surf. Coat. Technol.* **2018**, *340*, 210–221. [CrossRef]
34. Shao, G.; Lu, Y.; Hanaor, D.A.H.; Cui, S.; Jiao, J.; Shen, X. Improved oxidation resistance of high emissivity coatings on fibrous ceramic for reusable space systems. *Corros. Sci.* **2019**, *146*, 233–246. [CrossRef]
35. Monfort, F.; Matykina, E.; Berkani, A.; Skeldon, P.; Thompson, G.E.; Habazaki, H.; Shimizu, K. Species separation during coating growth on aluminium by spark anodizing. *Surf. Coat. Technol.* **2007**, *201*, 8671–8676. [CrossRef]
36. Daroonparvar, M.; Yajid, M.A.M.; Yusof, N.M.; Bakhsheshi-Rad, H.R. Preparation and corrosion resistance of a nanocomposite plasma electrolytic oxidation coating on Mg-1% Ca alloy formed in aluminate electrolyte containing titania nano-additives. *J. Alloys Compd.* **2016**, *688*, 841–857. [CrossRef]
37. Wang, L.; Zhang, G.H.; Chou, K.C. Study on oxidation mechanism and kinetics of MoO_2 to MoO_3 in air atmosphere. *Int. J. Refract. Met. Hard Mater.* **2016**, *57*, 115–124. [CrossRef]
38. Wang, P.; Li, J.P.; Guo, Y.C.; Yang, Z.; Wang, J.L. Ceramic coating formation on high Si containing Al alloy by PEO process. *Surf. Eng.* **2016**, *32*, 428–434. [CrossRef]
39. Dai, L.; Li, W.; Zhang, G.; Fu, N.; Duan, Q. Anti-corrosion and wear properties of plasma electrolytic oxidation coating formed on high Si content Al alloy by sectionalized oxidation mode. *J. Phys. Conf. Ser. Mater. Sci. Eng.* **2016**, *167*, 012063. [CrossRef]
40. Zhu, L.; Ke, X.; Zhang, B.; Zhang, Y.; Sui, M. Self-repairing capability of magnesium alloy during the plasma electrolytic oxidation process. *J. Alloys Compd.* **2018**, *766*, 88–94. [CrossRef]
41. Dur, A.; Castro, Y.; Milǒ, I. Self-Healing Effect of Hybrid Sol-Gel Coatings Based on GPTMS, TEOS, SiO_2 Nanoparticles and $Ce(NO_3)_3$ Applied on Aluminum Alloy 7075-T6. *J. Electrochem. Soc.* **2018**, *165*, 213–225. [CrossRef]
42. Lee, H.; Singh, J.K.; Ismail, M.A. An effective and novel pore sealing agent to enhance the corrosion resistance performance of Al coating in artificial ocean water. *Nat. Publ. Gr.* **2017**, *7*, 1–22. [CrossRef] [PubMed]
43. KIM, D.S.; SEGAWA, K.; SOEYA, T.; WACHSt, I.E. Surface Structures of Supported Molybdenum Oxide Catalysts under Ambient Conditions. *J. Catal.* **1992**, *136*, 539–553. [CrossRef]
44. Rosenfeld, L.; Danilov, I.S. Electrochemical aspects of pitting corrosion. *Corros. Sci.* **1967**, *7*, 129–142. [CrossRef]
45. Curioni, M.; Salamone, L.; Scenini, F.; Santamaria, M.; Di Natale, M. A mathematical description accounting for the superfluous hydrogen evolution and the inductive behaviour observed during electrochemical measurements on magnesium. *Electrochim. Acta* **2018**, *274*, 343–352. [CrossRef]
46. Gao, Y.; Yerokhin, A.; Matthews, A. Effect of current mode on PEO treatment of magnesium in Ca- and P-containing electrolyte and resulting coatings. *Appl. Surf. Sci.* **2014**, *316*, 558–567. [CrossRef]